PAPER

Check for updates

Influence of Sn doping on the optoelectronic properties of ZnO nanoparticles

Nadim Munna,[†ab] Rahim Abdur, [iD] [†b] Robiul Islam,[bc] Muhammad Shahriar Bashar, [iD] [b] Syed Farid Uddin Farhad, [iD] [d] Md. Kamruzzaman,[a] Shahin Aziz,[b] Md. Aftab Ali Shaikh,[ef] Mosharof Hossain [iD] [b] and Mohammad Shah Jamal [iD] [*b]

Zinc Oxide (ZnO) nanoparticles (NPs) obtained a lot of attention from researchers and industries because of their superior properties as an optoelectronic material. Doping, especially tin (Sn), can further fine-tune their optoelectronic properties. In this manuscript, we have reported the optoelectronic properties of Sn-doped ZnO NPs, which were synthesized by a simple chemical solution method. A wide range of dopant (Sn) concentrations were used in the ratios of 0, 1, 3, 5, 7, and 10 weight percent. The effects of dopant (Sn) concentration on the structural, morphological, elemental composition, and optical properties of ZnO NPs were investigated by using an X-ray diffractometer (XRD), Field Emission Scanning Electron Microscope (FESEM), X-ray photoelectron spectrometer (XPS) and UV-Vis-NIR respectively. XRD analysis revealed the shifting of diffraction patterns towards a higher angle along with decreasing intensity. The calculated crystallite size using the XRD varied from 40.12 nm to 28.15 nm with an increasing doping percentage. Sn doping notably influences the size of ZnO NPs, along with crystal quality, strain, and dislocation density. The X-ray photoelectron spectroscopy (XPS) study showed the presence of zinc (Zn), oxygen (O), and tin (Sn) with their preferred oxidation states in the synthesized NPs. UV-Visible spectroscopy (UV-Vis) showed that the bandgap changed from 3.55 to 3.85 eV with the increasing concentration of Sn. FE-SEM revealed that the structures and surfaces were irregular and not homogeneous. The above findings for ZnO nanostructures show their potential application in optoelectronic devices.

Introduction

As a member of the metal oxide family, ZnO has attained a lot of attention from the scientific community, because of its wide bandgap (>3 eV),[1] wide range conductivity,[2] higher exciton binding energy,[3,4] lower resistivity,[1,5] non-toxicity, higher transparency within the visible range, and higher light-trapping properties.[1,3,5] It has a hexagonal or wurtzite structure and the microstructure of ZnO has found numerous fundamental applications. Among them, the main application of ZnO at present is in photovoltaic applications,[6–8] UV photo-

detectors,[9] thin-film transistors,[10] photocatalysts of higher chemical activity, gas sensors,[11] and varistors.[12] ZnO semiconductors' electrical, optoelectronic, and piezoelectric properties can be tuned by various modification techniques. Along with these, different ZnO morphologies such as nanorods, nanotubes, nanoflowers, and nanowires offer exceptional opportunities to expand the range of applications. The development of UV lasers using ZnO nanorods has substantially accelerated research on ZnO nanorods and nanowires.[13] In this regard, the controlled morphology, growth factors, and physical attributes of such structures are now very popular with researchers. Sol–gel, direct precipitation, hydrothermal and microwave-assisted thermal oxidation, and other chemical and physical techniques have been reported to synthesize ZnO nanoparticles.[14,15] Most of the synthesis processes used hazardous chemicals, were expensive, required high temperatures, and took a long time to complete, all of which were shortcomings for industrial production.[16] Several factors affect the properties of ZnO NPs, such as the pH of the reaction mixture, reaction temperature, zinc salt precursors, reaction time, concentration of precursors, precipitating agents, calcination temperature, *etc.*[17]

The chemical solution process is one of the popular methods of synthesizing ZnO NPs, as in it, a simple precipitation method

aDepartment of Applied Chemistry and Chemical Engineering, University of Dhaka, Dhaka-1000, Bangladesh

bInstitute of Fuel Research and Development (IFRD), Bangladesh Council of Scientific and Industrial Research (BCSIR), Dr. Qudrat-E-Khuda Road, Dhanmondi, Dhaka-1205, Bangladesh. E-mail: msjdubd@gmail.com

cDepartment of Applied Chemistry and Chemical Engineering, Noakhali Science and Technology University, Noakhali-3814, Bangladesh

dBCSIR Laboratories Dhaka, Bangladesh Council of Scientific and Industrial Research (BCSIR), Dr. Qudrat-E-Khuda Road, Dhanmondi, Dhaka-1205, Bangladesh

eBangladesh Council of Scientific and Industrial Research (BCSIR), Dr. Qudrat-E-Khuda Road, Dhanmondi, Dhaka-1205, Bangladesh

fDepartment of Chemistry, University of Dhaka, Dhaka-1000, Bangladesh

† Nadim Munna and Rahim Abdur contributed equally to this work.

is used and requires simple chemicals.[17–21] In this process, the size, shapes, and purity are easily controllable by tuning fewer parameters. Mostly zinc salt precursors, the pH of the reaction mixture, and calcination temperature play a vital role in the properties of ZnO NPs. Mayekar *et al.*[22] reported that a zinc acetate precursor produces 39.91 nm spherical-shaped NPs with the highest purity compared to nitrate and chloride. In the case of the pH effect, lower pH values of the mixture produce larger crystals than higher pH values.[17] The calcination process helps to fuse and grow larger than its initial crystallite size.[23] Parra and Haque reported[24] that the size of ZnO NPs increases from 30 nm to 44 nm with the calcination temperature increasing from 200 °C to 500 °C.

Nevertheless, the properties of synthesized NPs require further fine-tuning depending on their applications. Considering the optoelectronic application of ZnO NPs, the optical band gap, energy band gap band alignment, electrical conductivity, and surface morphology needed to be fine-tuned based on the other material's properties of that device as well as its architecture. Doping with different elements influences the crystallite size as well as other physical, optical, and chemical properties. Appropriate dopant choosing is an important issue in tuning desired properties. For ZnO doping, Sn has become a suitable candidate because it is considered an n-type dopant for the doping of ZnO nanoparticles. The radius of Sn^{4+} is 0.071 nm which is similar to that of Zn^{2+} (0.074 nm) and this helps in the effective replacement of Zn ions.[1,2,12] Sn-doped ZnO can be effectively synthesized and its physical and chemical properties have been examined by several groups.[18,19,25–28] Still, a systematic study can enrich this vast topic and facilitate future improvements and fine-tuning.

In this study, we have synthesized ZnO and Sn-doped ZnO NPs using a simple chemical solution process. To ensure spherical-shaped NPs with the highest purity, we have used zinc acetate as the Zn precursor, stannic chloride as the Sn precursor, and NaOH as the precipitating agent. Also to ensure uniform interaction conditions among the precursors and understand only the doping effect we have mixed precursors at a fixed rate with a slow stirring rate of 400 rpm. The Sn-dopant concentrations were varied in the ratios of 0, 1, 3, 5, 7, and 10 weight (wt%) percent of ZnO solution. The synthesized NPs were investigated systematically to understand the Sn-doping effect on ZnO using different physical, chemical, optical, and electrical characterization methods. Based on the properties of the ZnO NPs, the suitability of their application in optoelectronic devices, especially in photovoltaic devices, is discussed.

Materials and methods

Materials

All solvents and chemicals were purchased and utilized without further purification. Zinc acetate dihydrate [$Zn(CH_3COO)_2 \cdot 2H_2O$] (≥98%), sodium hydroxide (NaOH) (≥98%), tin(IV) chloride pentahydrate ($SnCl_4 \cdot 5H_2O$) (≥98%), and 2-propanol (IPA) (extra pure) were purchased from Sigma-Aldrich Co. Whatman qualitative filter paper (110 mm $\varnothing$ × 100 circles) was purchased from a local vendor.

Synthesis of ZnO NPs

ZnO NPs with Sn doping were synthesized following a method known as the chemical solution method. 50 mM $Zn(CH_3COO)_2 \cdot 2H_2O$ and $SnCl_4 \cdot 5H_2O$ were prepared by dissolving 1.1075 g and 1.753 g in 100 mL of deionized water (DI) respectively. A 100 mM NaOH solution was also prepared by dissolving 0.4 g in 250 mL of DI. To synthesize ZnO NPs, 24 drops per minute of NaOH were added into the ($Zn(CH_3COO)_2 \cdot 2H_2O$) precursor solution until complete precipitation and the whole process was carried out under continuous magnetic stirring at 400 rpm. A white precipitate (ppts) of $Zn(OH)_2$ was formed. The ppts were filtered using Whatman qualitative filter paper and washed using DI until unreacted NaOH was removed. After that, the ppts were oven-dried at 60 °C for 24 h. Then the ppts were ground using a Pulverisette 23 (FRITSCH, Germany) at 50 Hz for 4 min with 10 balls (total 2.1 g). Finally, the ground NPs were calcined at 500 °C for 5 h to oxidize $Zn(OH)_2$ to ZnO. After cooling to room temperature, the ZnO NPs were used for different characterization methods.

In the case of Sn-doped ZnO NPs, 1, 3, 5, 7, and 10 wt% $SnCl_4 \cdot 5H_2O$ solution were added to ($Zn(CH_3COO)_2 \cdot 2H_2O$) solution and stirred at 400 rpm for 2 h to confirm the complete mixing. Then the same process as for the synthesis of only ZnO NPs was followed.

A 1.5 wt% dispersion solution of ZnO and Sn-doped ZnO NPs was made by dispersing 0.075 g of NPs in 5 mL of IPA using vigorous sonication (Digital ultrasonic cleaner, LABTRON) at 40 kHz for 30 min. Then the dispersion was allowed to stand for 5 min to cool down and spin-coated on pre-cleaned glass substrates at 3000 rpm for 30 s. Finally, the films were annealed on a hot plate for 10 min at 100 °C to remove the remaining solvent from the thin film.

Characterization

ZnO and Sn-doped ZnO NP powder crystallographic information was obtained using XRD (Cu Kα radiation, $\lambda = 0.15406$ nm, 40 kV and 60 mA, scanning range of 20–80°, and ARL Equinox 1000, Thermo Scientific™, USA), morphological information was achieved using Field Emission Scanning Electron Microscopy (FE-SEM) (JEOL-7610F, Japan), and elemental composition was observed by Energy Dispersive Spectroscopy (EDS) coupled with FE-SEM (JEOL-7610F, Japan) and Scanning Electron Microscopy (SEM) (Carl Zeiss AG, EV018, UK). ZnO and Sn-doped ZnO NP thin films prepared on a glass substrate were used to characterize compositional information with the chemical state using X-ray photoelectron spectroscopy (XPS, K-alpha, Thermo Scientific™, USA), and optical transmission with an optical bandgap was characterized using UV-Visible spectroscopy (UH4150 Spectrophotometer (Integrating Sphere), Hitachi, Japan) from 280 nm to 800 nm at a 600 nm per minute scanning rate. Electrical properties were acquired using a Hall measurement equipment (Ecopia Corp., HMD-3000, South Korea). Inductively Coupled Plasma Mass Spectroscopy (ICP-MS) (PerkinElmer, Model: NexION 2000) was used to further analyze Zn and Sn contents in the prepared NPs.

Results and discussion

Structural properties

The XRD patterns of the NP powders are shown in Fig. 1. Sharp diffraction peaks (2θ) are located at 31.84°, 34.52°, 36.28°, 47.5°, 56.65°, 62.87°, 68.00°, 69.13°, 72.62°, 77.06°, and 81.47° attributed respectively to the (100), (002), (101), (102), (110), (103), (200), (112), (201), and (004) crystal planes of the hexagonal close-packed (HCP) ZnO structure (JCPDS card no. 01-1136).[29] No other diffraction patterns related to SnO_2 or any other impurities were not observed even at 10% doping concentration.

With the increase in the Sn doping percentage, all the reflections' intensity decreased. This effect is mainly due to the difference in ionic radii between the Zn and the dopant Sn.[30] The smaller ionic radii Sn^{4+} (0.69 Å), substitutes Zn^{2+} (0.69 Å) or insert into the vacant Zn^{2+} sites in the ZnO lattice. This smaller-sized Sn^{4+} makes stronger interaction with O^{2-} in the lattice,[12,31] which induces strain in the lattice leading to FWHM broadening with intensity reduction of all the diffraction patterns. This substitution or insertion was not site-selective, so several diffraction patterns shifted with increasing doping percent. All the samples showed a preferred orientation towards the (101) diffraction plane. The reflection position shifting of the (101) plane, full width at half maxima (FWHM) values of the (101) plane, crystallite size, microstrain, and dislocation density variation with the doping percentage are listed in Table 1.
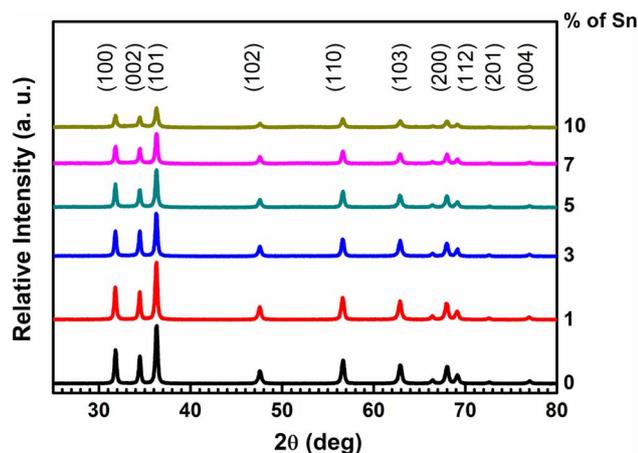
Table 1 column 2 shows the continuous shifting of the (101) plane towards a higher angle with the increase of the Sn doping percentage to ZnO, indicating that Sn^{4+} can replace Zn^{2+} ions without altering the crystal structure.[30] The crystallite size of the un-doped and Sn-doped ZnO NPs was calculated from the XRD data using Debye–Scherrer's formula.[32] The equation is:

$$D = \frac{K\lambda}{\beta \cos \theta} \tag{1}$$

where λ is the wavelength (1.5406 Å), β is the FWHM of the peak, and θ is the diffraction angle obtained from the 2θ value of the peak. The crystallite size (D) has been calculated for the highest intensity peak along the (101) plane. Column 4 shows the crystallite size variation with the doping concentration. The crystallite size of un-doped, 1%, 3%, 5%, 7%, and 10% Sn-doped ZnO NPs is 40.73 nm, 38.38 nm, 36.43 nm, 33.06 nm, 32.60, and 28.08 nm respectively. Sn-doped ZnO NPs' crystallite size decreased as the Sn doping concentration increased. Thus the microstrain and dislocation density trends increase with the increasing doping percentage of Sn.

Morphology study

The FE-SEM morphological images of pure ZnO and Sn-doped ZnO NPs are shown in Fig. 2. The images vividly depict the morphological changes caused by various amounts of Sn doping in ZnO. The nature is inhomogeneous when it comes to Sn-doped ZnO NPs.

Microstructural deviations demonstrate the method of nucleation development when the doping rate is increased.[12] Sn atoms cause these fluctuations by promoting rapid nucleation leading to the reduction of the particle size, by which the microstructure is relaxed and lowers the energy of the system. Additionally, the surface revealed that Sn doping has a significant impact. Sn mainly modifies and enhances the ZnO NP structure.[12] The most important component in determining the final product's shape and structure was the Sn ratio. Several microstructure sizes were measured to predict the average microstructure size of the synthesized NPs. The microstructure size was 45.58 ± 7.11, 39.13 ± 6.22, 38.08 ± 4.75, 35.44 ± 1.71, 34.46 ± 3.04, and 27.38 ± 4.92 nm for 0, 1, 3, 5, 7, and 10 wt% Sn doping into ZnO NPs respectively. These data show a similar tendency to the XRD-derived crystallite size data.

Fig. 1 Variation of the XRD pattern of ZnO NPs with the Sn doping percentage.

Table 1 Extracted physical properties of the synthesized Sn-doped ZnO NPs using the (101) plane of Fig. 1

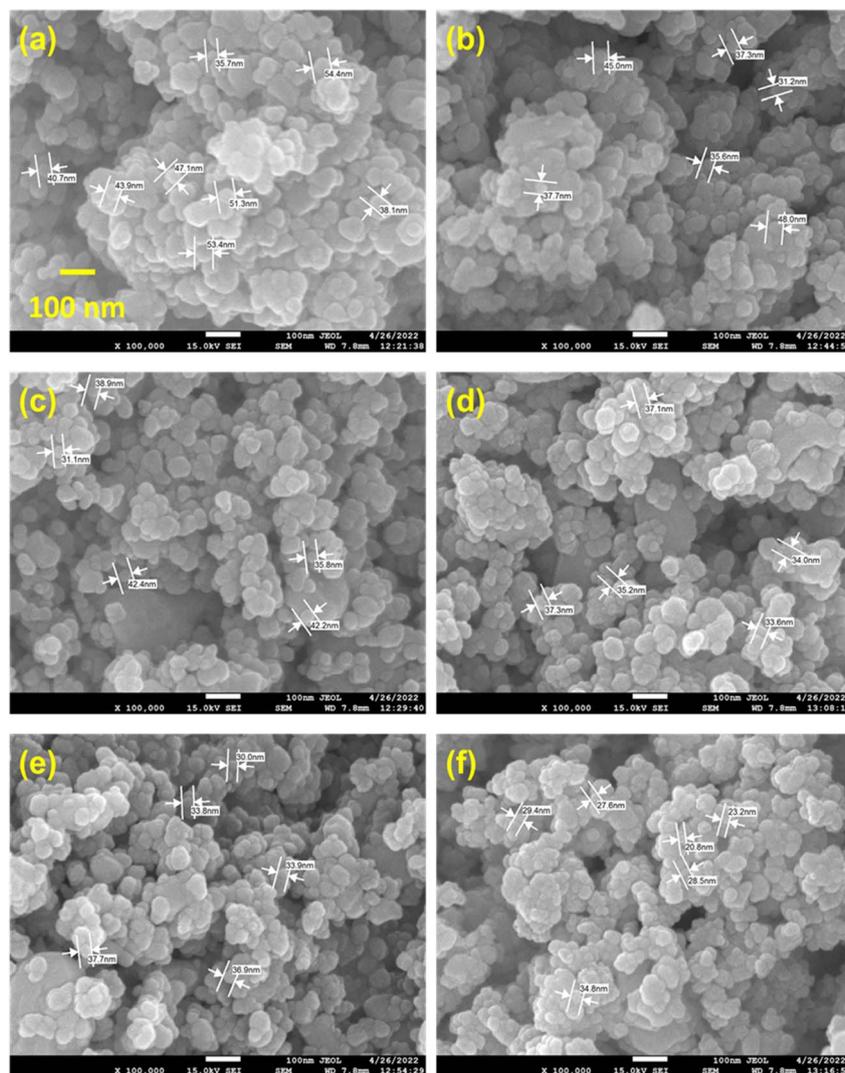| Doping percentage (%)	Peak position (degree)	FWHM (degree)	Crystallite size (nm)	Microstrain × 10^{-3} (%)	dislocation density (m^{-2})
0	36.21	0.23	40.73	3.04	0.60
1	36.24	0.24	38.38	3.23	0.68
3	36.29	0.26	36.43	3.40	0.75
5	36.35	0.28	33.06	3.73	0.91
7	36.41	0.28	32.60	3.78	0.94
10	36.47	0.33	28.08	4.38	1.27

Fig. 2 FE-SEM morphological image of the synthesized Sn-doped ZnO NPs with (a) 0, (b) 1, (c) 3, (d) 5, (e) 7, and (f) 10 wt% doping percent.

Electrical properties

The electrical properties of the pure ZnO and Sn-doped ZnO thin films, fabricated from the synthesized NPs, were carried out using the van der Pauw method.[33] All the films showed n-type semiconductor behavior. The bulk carrier concentration for the pure ZnO thin film was found to be 2.46×10^{11} cm^{-3} and increased with Sn doping concentration up to 3.03×10^{13} cm^{-3} for 10% Sn doping. Fig. 3(a) illustrates the carrier concentration variation with Sn doping concentration. As the Sn^{4+} ion substitutes the Zn^{2+} ion in the ZnO lattice or inserts in the vacant sites of the lattice, it creates extra free electrons increasing the bulk carrier concentration. In the case of mobility, trends decrease with increasing Sn doping concentration, as illustrated in Fig. 3(b). As doping increases the bulk density increase leading to a decrease in mobility. On the other hand, the resistivity of the thin films (Fig. 3(c)) decreased up to 9.60×10^2 Ω cm for 5% Sn doping from 1.46×10^4 Ω cm for pure ZnO and then increased again for further doping.

Optical properties

The optical transmittance spectra for pure ZnO with Sn-doped nanostructured thin films are shown in Fig. 4(a) for wavelengths ranging from 300 to 800 nm. According to this graph, all the films were highly transparent in the visible range with a rapid reduction in the UV region, which is somewhat moved to lower wavelengths with the Sn doping percentage increasing. The mean optical transmittance throughout the visible region for pure ZnO thin films was about 87%, with an absorption edge at approximately 369 nm (Fig. 4(a)). Sn-doped ZnO NPs displayed better transparency than pure ZnO NPs, as shown in Fig. 4(a). Furthermore, the average transmittances of 1 wt% doped films were lower than those of pure films. This conclusion is consistent with surface roughness assessments. According to Lee et al.,[34] the reduced transmittance in Sn-doped ZnO thin films could be due to increased optical scattering generated by their rough surface morphology. In this work, the 10 wt% Sn-doped ZnO thin film had the highest transparency
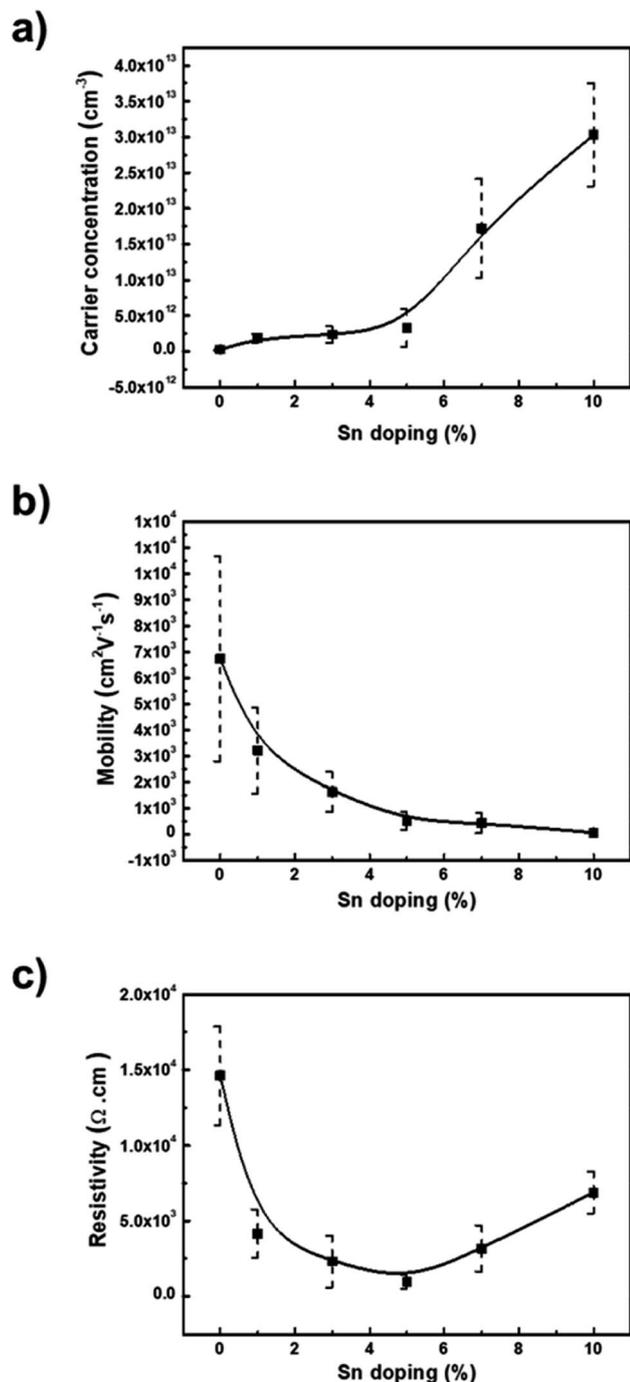
Fig. 3 (a) Carrier concentration variation of the bulk ZnO NP thin films, (b) mobility of free carriers in the ZnO NP thin films, and (c) resistivity variation of the ZnO NP thin film with the Sn doping percent.

amongst the doped samples, with 98.65 percent average transparency.

The optical band gap of pure ZnO (Fig. 4(b)) and Sn-doped ZnO (Fig. 4(c)) NP thin films is computed from the Tauc plot between $h\nu$ (eV) and $(\alpha h\nu)^2$. The following well-known equation is used to compute the direct optical bandgap:

$$(\alpha h\nu)^{1/n} = B(h\nu - E_g) \tag{2}$$

where α is the absorption coefficient, B is a constant, $h\nu$ is the photon energy and E_g is the optical bandgap energy, and 'n' is an index.[18] During the band gap computation, it is discovered that for $n = 2$, eqn (2) provides the best linear fit on the projection of the Tauc plot. The computed band gap for pure ZnO is 3.55 eV, whereas the band gap for 1, 3, 5, 7, and 10 wt% Sn-doped ZnO NPs is 3.72, 3.74, 3.79, 3.81, and 3.85 eV, respectively. The optical band gap increases with the Sn doping percent, as Sn^{4+} substitutes Zn^{2+} or inserts in the vacant site of Zn^{2+} of the ZnO lattice leading to an increase in carrier concentration and a decrease in carrier mobility. This causes the Fermi level to move towards the conduction band caused by the Burstein–Moss shift.[35] These results were justified by the electrical properties of the prepared films. The optical bandgap variation with increasing Sn doping percentage is shown in Fig. 5. Similar results were reported by Munguti et al.[36]

This optical band gap tuning of Sn-doped ZnO NPs enables the suitability of applying them in various optoelectronic devices[37] including photovoltaics.

Compositional analysis

The EDS analysis of pure ZnO and Sn-doped ZnO NPs is illustrated in Fig. 6. Pure ZnO NPs showed only Zn and O elemental peaks (Fig. 6(a)). On the other hand, Sn-doped ZnO NPs showed Zn, Sn, and O elemental peaks (Fig. 6(b–f)). The Sn atomic percent increased with increasing Sn doping percent, though the atomic percent does not directly depict the original doping percent, but rather illustrates the doping increasing trend.

To check the Sn atomic percent present in the ZnO NPs, the samples were further characterized with ICP-MS. The sample was digested with HCl. The processed acid digested samples were directly analyzed using an ICP-MS. The data from the ICP-MS were processed with Syngistix™ software for their heavy metal contents following the process reported by Roychowdhuri et al.[38] The glassware utilized in this experiment underwent a thorough cleaning process, involving ultrapure acid and water, to minimize the potential for contamination during both sample preparation and analytical procedures. Prior to calibration with standards, the performance of the ICPMS equipment was assessed using a NexION Setup solution from PerkinElmer, USA. A calibration variance of five points was successfully achieved, with an R^2 value > 0.9995. To ensure the stability of the instrument, a minimum of three replicates were performed. A maximum relative standard deviation (RSD) of 5–8% was taken into consideration. The detection (DL) and quantification (QL) limits of the instrument were established by determining the point at which the signal for a particular metal exceeded the background noise by three and ten times, respectively. The quality control process involved the execution of procedures, determination of SRM recoveries, and assessment of spike recoveries in order to mitigate potential errors. The concentrations of trace metals were adjusted based on recoveries and blank sample analysis. The average values with standard deviation are presented in Table 2.
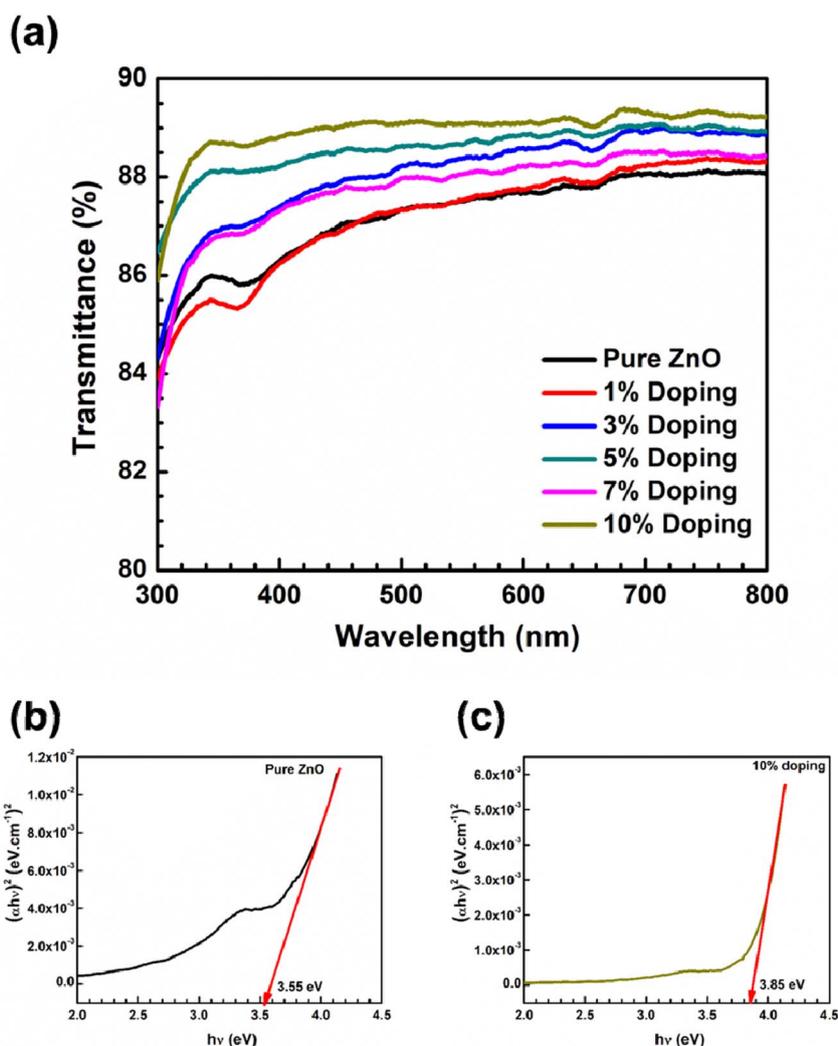
Fig. 4   (a) Transmittance of the Sn-doped ZnO NP thin films fabricated on bare glass, and Tauc plot of (b) pure ZnO NPs, and (c) 10 wt% Sn-doped ZnO NPs used to calculate the optical bandgap.
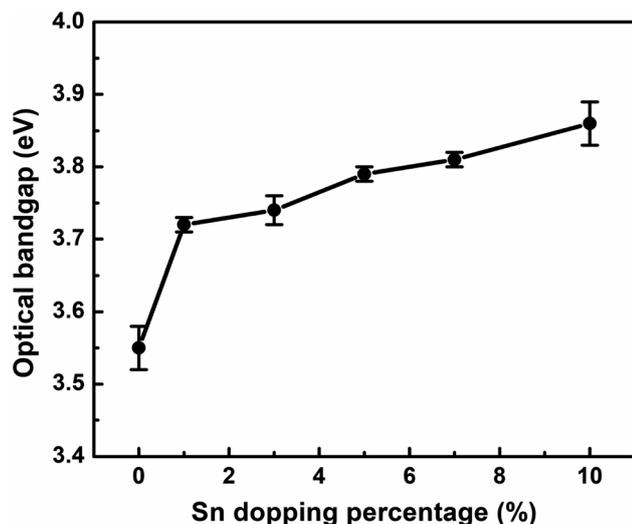

Fig. 5   Optical bandgap variation of Sn-doped ZnO NPs with the Sn doping percentage.

The XPS spectra of 5 wt% Sn-doped ZnO NPs are shown in Fig. 7. The presence of zinc (Zn), oxygen (O), and tin (Sn) is indicated by the presence of obvious Zn 2p, O 1s, and Sn 3d peaks. The binding energies were measured using the C 1s peak as a benchmark (284.5 eV). All the data were deconvoluted using simulation software XPSPEAK41. Black lines represent raw data, dotted red lines represent simulated data, and other colored lines represent deconvoluted peaks to fit the simulated data in Fig. 7. The binding energies of the deconvoluted Zn 2p spectral peaks (Fig. 7(a)) are 1021.9 eV and 1044.8 eV, for Zn $2p_{3/2}$ and Zn $2p_{1/2}$, respectively, with the corresponding satellite peaks.

which confirm the presence of ZnO.[30] The deconvoluted O 1s spectrum (Fig. 7(b)) showed peaks at 531.1 and 530.6 eV, confirming the presence of ZnO and SnO_2 respectively.[30] Finally, the spectral peak of Sn 3d (Fig. 7(c)) is deconvoluted into two peaks. The peaks at 487.08 and 483.98 eV represent Sn $3d_{5/2}$ and its satellite peak respectively for SnO_2.[30] These results confirm the successful Sn doping of ZnO.
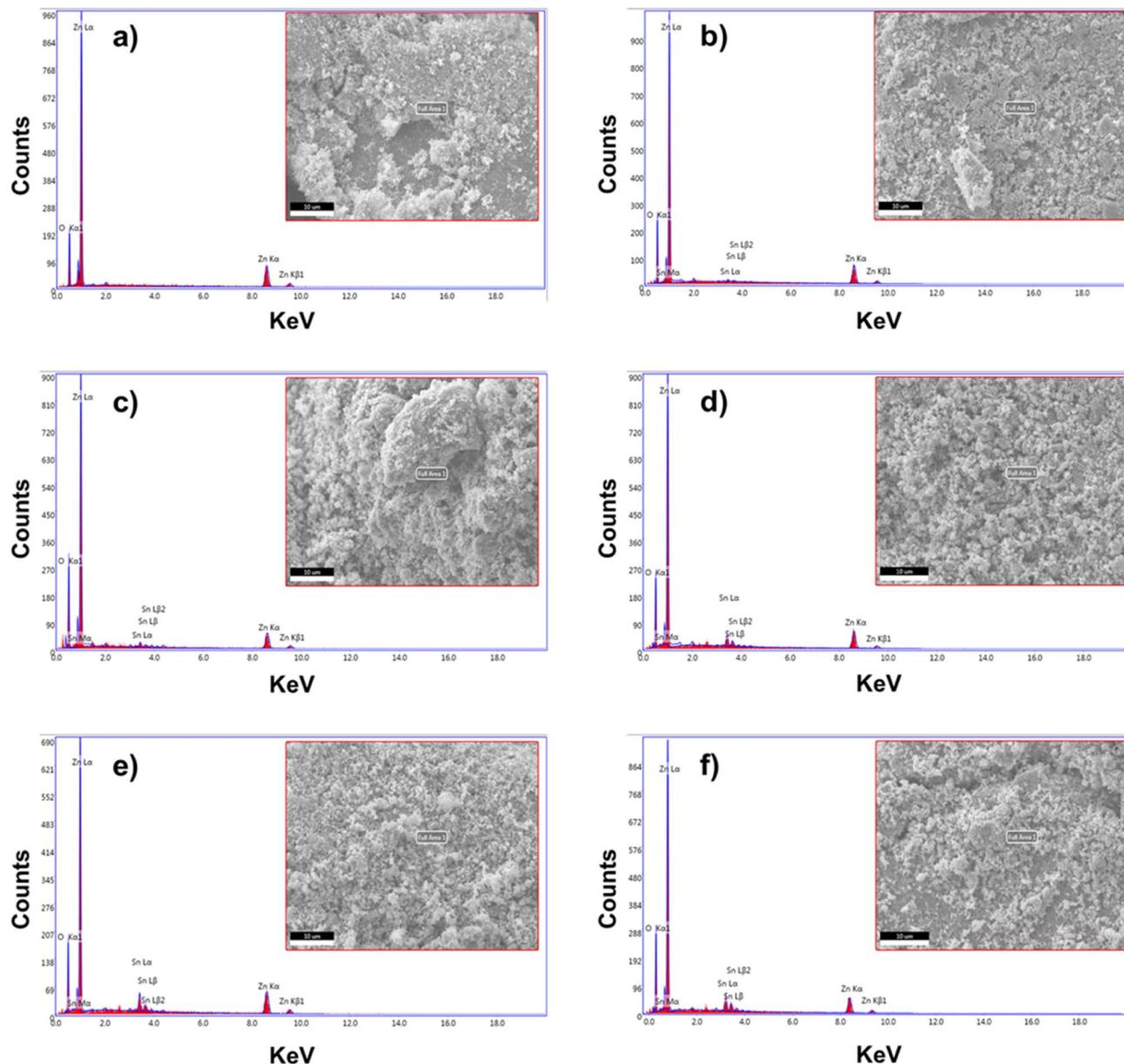
Fig. 6 SEM morphological image with EDS mapping of the synthesized Sn-doped ZnO NPs with (a) 0, (b) 1, (c) 3, (d) 5, (e) 7, and (f) 10 wt% doping percent.

Table 2 Elemental composition of pure ZnO and Sn-doped ZnO NPs obtained by EDS analysis and ICP-MS

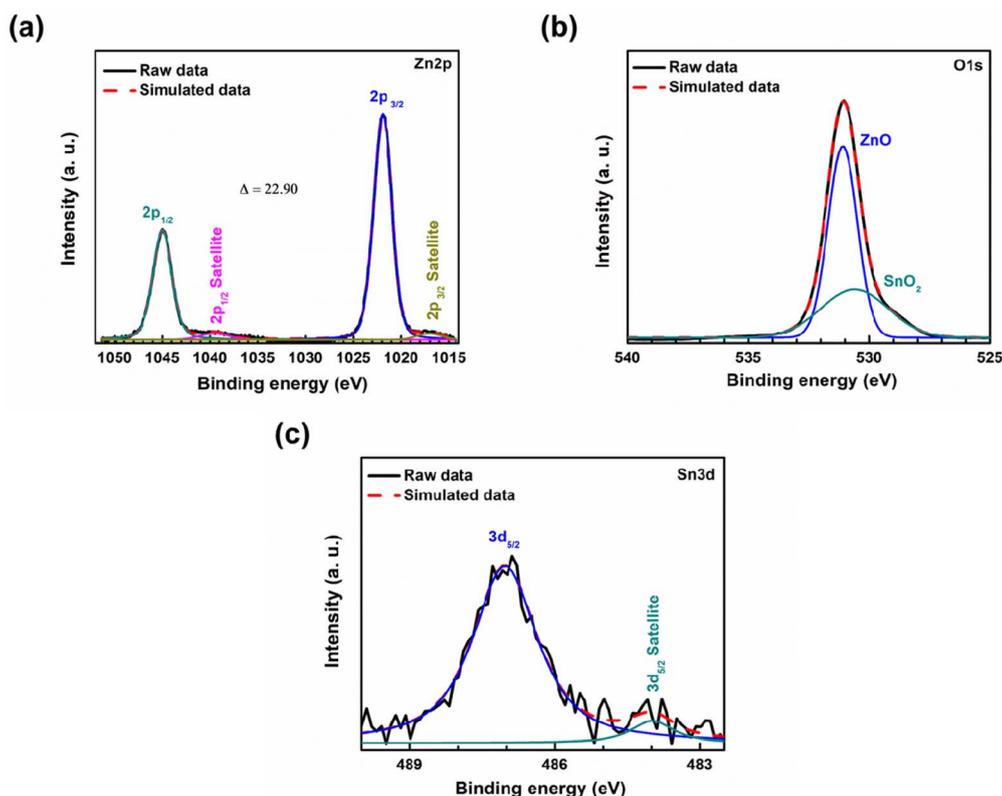|	Atomic percentage (%)				
	EDS			ICP-MS	
Sample	Zn	Sn	O	Zn	Sn
Pure ZnO	60.23 ± 5.30	Not detected	39.77 ± 5.30	79.66 ± 0.65	Not detected
1% Sn doped ZnO	55.20 ± 2.76	0.45 ± 0.17	44.35 ± 2.82	79.12 ± 1.28	0.87 ± 0.04
3% Sn doped ZnO	63.79 ± 25.47	1.01 ± 0.45	35.19 ± 25.04	77.84 ± 0.57	2.77 ± 0.14
5% Sn doped ZnO	59.52 ± 14.71	3.04 ± 1.53	37.44 ± 13.18	76.69 ± 0.63	4.86 ± 0.32
7% Sn doped ZnO	51.52 ± 6.65	4.60 ± 1.00	43.89 ± 6.98	74.54 ± 0.76	6.74 ± 0.14
10% Sn doped ZnO	46.72 ± 2.91	5.96 ± 1.64	47.32 ± 1.75	71.90 ± 0.37	9.37 ± 0.47

Fig. 7 Deconvoluted XPS spectra of (a) Zn 2p, (b) O 1s, and (c) Sn 3d of 5 wt% Sn-doped ZnO NPs.

Conclusions

Tin (Sn) doped zinc oxide (ZnO) NPs were synthesized by a simple chemical solution process. It was found that doping of Sn significantly altered the morphology of ZnO NPs, confirmed by FE-SEM. Sn doping has a notable influence on the size of ZnO NPs, as well as the crystal quality, microstrain, and dislocation density of ZnO nanoparticles, according to data analyzed by XRD. An XPS study showed the presence of Zn, O, and Sn elements in the 5 wt% Sn-doped ZnO NPs. Also, the binding energy of these elements confirmed the Zn^{2+} substitution by Sn^{4+} in the Sn-doped ZnO NPs. UV-Visible spectroscopy revealed that the band gap increases with the increasing concentration of Sn. Meanwhile the electrical properties revealed the lowest resistivity of 9.60×10^2 Ω cm for the 5% Sn-doped ZnO NP thin film with an optical band gap of 3.79 eV. These wide band gap Sn-doped ZnO NPs can be suitable for optoelectronic applications such as photovoltaic devices.

Author contributions

N. M.: data curation, formal analysis, investigation, validation, and writing-original draft. R. A.: data curation, formal analysis, investigation, methodology, visualization, validation, supervision, and writing-review & editing. R. I.: data curation and validation. S. F. U. F.: investigation and validation. M. K.: writing-review & editing. S. A.: writing-review & editing. M. A. S. A.: writing-review & editing. M. H.: supervision, writing-review & editing, and funding acquisition. M. S. J.: conceptualization, funding acquisition, project administration, validation, supervision, and writing – review & editing.

Conflicts of interest

The authors declare that they have no conflict of interest.

Acknowledgements

References

1 S. Ameen, M. S. Akhtar, H. K. Seo, Y. S. Kim and H. S. Shin, *Chem. Eng. J.*, 2012, **187**, 351–356.

2 C. Y. Tsay, H. C. Cheng, Y. T. Tung, W. H. Tuan and C. K. Lin, *Thin Solid Films*, 2008, **517**, 1032–1036.

3 S. Fiedler, L. O. L. C. Lem, C. Ton-That, M. Schleuning, A. Hoffmann and M. R. Phillips, *Sci. Rep.*, 2020, **10**, 1–9.

4 D. G. Thomas, *J. Phys. Chem. Solids*, 1960, **15**, 86–96.

5 Y. Caglar, S. Aksoy, S. Ilican and M. Caglar, *Superlattices Microstruct.*, 2009, **46**, 469–475.

6 L. Lin and N. M. Ravindra, *Emerging Mater. Res.*, 2020, **9**, 812–824.

7 I. Repins, M. A. Contreras, B. Egaas, C. DeHart, J. Scharf, C. L. Perkins, B. To and R. Noufi, *Prog. Photovoltaics*, 2008, **16**, 235–239.

8 J. Ramanujam, D. M. Bishop, T. K. Todorov, O. Gunawan, J. Rath, R. Nekovei, E. Artegiani and A. Romeo, *Prog. Mater. Sci.*, 2020, **110**, 100619.

9 M. R. Hasan, T. Xie, S. C. Barron, G. Liu, N. V. Nguyen, A. Motayed, M. V. Rao and R. Debnath, *APL Mater.*, 2015, **3**, 106101.

10 S. Lee, Y. Jeong, S. Jeong, J. Lee, M. Jeon and J. Moon, *Superlattices Microstruct.*, 2008, **44**, 761–769.

11 S. Kumar, V. Singh and A. Tanwar, *J. Mater. Sci.: Mater. Electron.*, 2016, **27**, 2166–2173.

12 M. Arshad Javid, M. Rafi, I. Ali, F. Hussain, M. Imran and A. Nasir, *Mater. Sci. Polym.*, 2016, **34**, 741–746.

13 R. Zhang, P.-G. Yin, N. Wang and L. Guo, *Solid State Sci.*, 2009, **11**, 865–869.

14 S. Musić and A. Šarić, *Ceram. Int.*, 2012, **38**, 6047–6052.

15 S.-H. Yu, J. Yang, Y.-T. Qian and M. Yoshimura, *Chem. Phys. Lett.*, 2002, **361**, 362–366.

16 K. Handore, S. Bhavsar, A. Horne, P. Chhattise, K. Mohite, J. Ambekar, N. Pande and V. Chabukswar, *J. Macromol. Sci., Part A: Pure Appl.Chem.*, 2014, **51**, 941–947.

17 E. Y. Shaba, J. O. Jacob, J. O. Tijani and M. A. T. Suleiman, *Appl. Water Sci.*, 2021, **11**, 48.

18 M. Kahouli, A. Barhoumi, A. Bouzid, A. Al-Hajry and S. Guermazi, *Superlattices Microstruct.*, 2015, **85**, 7–23.

19 M. K. Debanath and S. Karmakar, *Mater. Lett.*, 2013, **111**, 116–119.

20 H. Ghorbani, F. Mehr, H. Pazoki and B. Rahmani, *Orient. J. Chem.*, 2015, **31**, 1219–1221.

21 G. Taka and T. D. Das, *IOP Conf. Ser.: Earth Environ. Sci.*, 2022, **1042**, 012017.

22 S. Mayekar, J. Dhar, V. Radha, *et al.*, *Int. J. Res. Eng. Technol.*, 2014, **03**, 43–45.

23 A. Ruys, in *Alumina Ceramics*, Elsevier, 2019, pp. 473–499.

24 M. R. Parra and F. Z. Haque, *J. Mater. Res. Technol.*, 2014, **3**, 363–369.

25 E. K. Droepenu, *Biointerface Res. Appl. Chem.*, 2022, **12**, 4261–4292.

26 P. M. Aneesh, K. A. Vanaja and M. K. Jayaraj, in *Nanophotonic Materials IV*, eds., Z. Gaburro and S. Cabrini, SPIE, 2007, vol. 6639, p. 66390J.

27 S. Arya, P. Mahajan, S. Mahajan, A. Khosla, R. Datt, V. Gupta, S.-J. Young and S. K. Oruganti, *ECS J. Solid State Sci. Technol.*, 2021, **10**, 023002.

28 H. Mirzaei and M. Darroudi, *Ceram. Int.*, 2017, **43**, 907–914.

29 J. D. Hanawalt, H. W. Rinn and L. K. Frevel, *Ind. Eng. Chem. Anal. Ed.*, 1938, **10**, 457–512.

30 M. Jung, S. Kim and S. Ju, *Opt. Mater.*, 2011, **33**, 280–283.

31 M. Verma, P. K. Dwivedi and B. Das, *J. Exp. Nanosci.*, 2015, **10**, 438–448.

32 T. Fukumura, Z. Jin, A. Ohtomo, H. Koinuma and M. Kawasaki, *Appl. Phys. Lett.*, 1999, **75**, 3366–3368.

33 F. S. Oliveira, R. B. Cipriano, F. T. da Silva, E. C. Romão and C. A. M. dos Santos, *Sci. Rep.*, 2020, **10**, 16379.

34 J.-H. Lee and B.-O. Park, *Thin Solid Films*, 2003, **426**, 94–99.

35 T. S. Moss, *Proc. Phys. Soc., London, Sect. B*, 1954, **67**, 775–782.

36 W. K. Munguti, L. K. Musembi, R. J. Njoroge, *et al.*, *Elixir Thin Film Technol.*, 2013, **61**, 17162–17165.

37 K. Saravanakumar, P. Sakthivel and R. K. Sankaranarayanan, *Spectrochim. Acta, Part A*, 2022, **267**, 120487.

38 T. Roychowdhury, T. Uchino, H. Tokunaga and M. Ando, *Food Chem. Toxicol.*, 2002, **40**, 1611–1621.